

Article

Highly Dispersed Pt-Incorporated Mesoporous Fe₂O₃ for Low-Level Sensing of Formaldehyde Gas

Seung Jin Jeon ^{1,2,†}, Kyung Hee Oh ^{3,4,†}, Youngbo Choi ^{2,*}, Ji Chan Park ^{3,5,*}  and Hyung Ju Park ^{1,*}

¹ Electronics and Telecommunications Research Institute (ETRI), 218 Gajeong-ro, Yuseong-gu, Daejeon 34129, Republic of Korea

² Department of Safety Engineering, Chungbuk National University, Cheongju 28644, Republic of Korea

³ Clean Fuel Research Laboratory, Korea Institute of Energy Research, Daejeon 34129, Republic of Korea

⁴ Department of Chemistry, Korea University, Seoul 02841, Republic of Korea

⁵ Energy Engineering, University of Science and Technology, Daejeon 34113, Republic of Korea

* Correspondence: ybc@cbnu.ac.kr (Y.C.); jcpark@kier.re.kr (J.C.P.); park77@etri.re.kr (H.J.P.)

† These authors contributed equally to this work.

Abstract: Highly dispersed Pt-incorporated mesoporous Fe₂O₃ (Pt/m-Fe₂O₃) of 4 μm size is prepared through a simple hydrothermal reaction and thermal decomposition procedures. Furthermore, the formaldehyde gas-sensing properties of Pt/m-Fe₂O₃ are investigated. Compared with our previous mesoporous Fe₂O₃-based gas sensors, a gas sensor based on 0.2% Pt/m-Fe₂O₃ shows improved gas response by over 90% in detecting low-level formaldehyde gas at 50 ppb concentration, an enhanced selectivity of formaldehyde gas, and a lower degradation of sensing performance in high-humidity environments. Additionally, the gas sensor exhibits similar properties as the previous sensor, such as operating temperature (275 °C) and long-term stability. The enhancement in formaldehyde gas-sensing performance is attributed to the attractive catalytic chemical sensitization of highly dispersed Pt nanoparticles in the mesoporous Fe₂O₃ microcube architecture.

Keywords: formaldehyde gas sensor; Pt-incorporated mesoporous Fe₂O₃; high sensitivity



Citation: Jeon, S.J.; Oh, K.H.; Choi, Y.; Park, J.C.; Park, H.J. Highly Dispersed Pt-Incorporated Mesoporous Fe₂O₃ for Low-Level Sensing of Formaldehyde Gas. *Nanomaterials* **2023**, *13*, 659. <https://doi.org/10.3390/nano13040659>

Academic Editors: Sergei Kulinich and Antonios Kelarakis

Received: 11 January 2023

Revised: 3 February 2023

Accepted: 4 February 2023

Published: 8 February 2023



Copyright: © 2023 by the authors. Licensee MDPI, Basel, Switzerland. This article is an open access article distributed under the terms and conditions of the Creative Commons Attribution (CC BY) license (<https://creativecommons.org/licenses/by/4.0/>).

1. Introduction

Among the various air pollutants, formaldehyde (HCHO) is a highly toxic substance which is commonly used in industries such as building construction and furniture [1,2]. Furthermore, due to its high toxicity, widespread distribution, and volatility, HCHO is a major cause of sick building syndrome (SBS). It is therefore classified as an indoor and outdoor air pollutant that poses a significant risk to human health [3,4], and the long-term exposure limit for HCHO has been set at a very low concentration. The Agency for Toxic Substances and Disease Registry (ATSDR) developed the minimal risk levels (MRLs) of HCHO at 40 ppb (1–14 days), 30 ppb (>14–364 days), and 8 ppb (≥365 days) [5]. Developing highly sensitive, stable, and selective gas sensors at these very-low-ppb-level concentrations of HCHO gas is thus crucial.

HCHO gas sensors based on metal oxide semiconductors are widely used because of their simple working principle, high sensitivity, portability, and low cost [6–11]. Additionally, a gas sensor based on p-type mesoporous metal oxide semiconductors, which conduct through positive-hole accumulation layers, provides a promising practical material platform for the low-level sensing of volatile organic compounds (VOCs), showing improved sensitivity, good selectivity, and lower humidity dependence [12–16].

Recently, well-designed metal oxide nanostructures with high surface area to volume ratios have been developed and applied to achieve effective gas sensing [17–19]. Furthermore, surface modification of the metal oxide structure by noble metals with unique electronic states and chemical properties has reduced the activation energy of adsorption and enhanced electron transfer efficiency, resulting in an improvement in gas-sensing

performance [20–22]. The loading of appropriate Pt dopant in mesoporous semiconductor materials has been shown to improve the performance of gas sensors [23–27]. However, obtaining the optimal dopant ingredients and amounts while maintaining the consistent mesoporous structure with enhanced gas-sensing properties is challenging. Additionally, the incorporation of highly dispersed Pt nanoparticles (NPs) has been limited by the complex procedures involved with harmful chemicals and inhomogeneous dispersion [28–32].

In this study, we introduce a novel formaldehyde (HCHO) gas-sensing material consisting of Pt NPs and a mesoporous Fe_2O_3 (m- Fe_2O_3) structure, which is prepared by the thermal oxidation of cubic-shaped $\text{FeC}_2\text{O}_4 \cdot 2\text{H}_2\text{O}$ particles as Fe_2O_3 precursors, and subsequently the additive thermal decomposition of $\text{Pt}(\text{acac})_2$ as a precursor of Pt NPs. The Pt-incorporated mesoporous Fe_2O_3 (Pt/m- Fe_2O_3) shows better sensitivity (Response: 2.13 at 50 ppb HCHO) than m- Fe_2O_3 , excellent selectivity for formaldehyde gas, and a long-term stability of 120 days, even at high humidity.

2. Methods

2.1. Chemicals

Iron (III) nitrate nonahydrate ($\text{Fe}(\text{NO}_3)_3 \cdot 9\text{H}_2\text{O}$, ACS reagent, $\geq 98\%$), poly (vinyl pyrrolidone) (PVP, Mw = 55,000), D-(+)-glucose (ACS reagent, $\geq 99.5\%$), and platinum (II) acetylacetonate ($\text{Pt}(\text{C}_5\text{H}_7\text{O}_2)_2$, $\text{Pt}(\text{acac})_2$, 97%) were purchased from Aldrich (St. Louis, United States). All reagents were used as received without further purification.

2.2. Synthesis of Pt-Incorporated Mesoporous Fe_2O_3 (Pt/m- Fe_2O_3) Microcubes

For the synthesis of Pt/m- Fe_2O_3 particles, m- Fe_2O_3 powder was prepared with a simple thermal decomposition of the cubic-shaped $\text{FeC}_2\text{O}_4 \cdot 2\text{H}_2\text{O}$, which could be obtained with a hydrothermal reaction, as in a previous report [33]. $\text{FeC}_2\text{O}_4 \cdot 2\text{H}_2\text{O}$ powders were thermally treated at 400 °C under a continuous flow of air ($200 \text{ mL} \cdot \text{min}^{-1}$) to yield m- Fe_2O_3 powder. For the incorporation of Pt NPs, m- Fe_2O_3 (0.5 g) and $\text{Pt}(\text{acac})_2$ (2.0 mg) were homogeneously mixed by grinding the powders in a mortar for 5 min under ambient conditions. Subsequently, the mixture was transferred to an alumina boat in a tube-type furnace, and then heated with a ramp of $3.3 \text{ }^\circ\text{C} \cdot \text{min}^{-1}$ to 400 °C. The final Pt/m- Fe_2O_3 powder was obtained by thermal treatment at 400 °C for 30 min under N_2 flow ($200 \text{ mL} \cdot \text{min}^{-1}$).

2.3. Characterization

Scanning electron microscope (SEM) images were obtained using a NovaNano SEM 450 (FEI, Hillsboro, OR, USA) by a Schottky field emission gun at 0.2–30 kV range with 1.0 nm ultimate resolution at 15 kV. A Talos F200X (Thermo Fisher Scientific, Waltham, MA, USA) with a 0.12 nm TEM information limit and a 0.16 nm STEM high-angle annular dark field (HAADF) resolution was used at 200 kV for transmission electron microscopy (TEM) analysis. Energy-dispersive X-ray spectroscopy (EDS) elemental mapping was performed using a high-efficiency detection system (Super X: 4 windowless SDD EDS system). The TEM samples were prepared by placing a few drops of the colloidal solutions on copper grids coated with Formvar carbon film (Ted Pella, Inc., Redding, CA, USA). Additionally, X-ray diffraction (XRD) patterns were measured on a Rigaku SmartLab X-ray diffractometer (Rigaku Corp., Tokyo, Japan) with Cu $K\alpha$ radiation ($\lambda = 1.54051 \text{ \AA}$), with a scan speed of $3^\circ \cdot \text{min}^{-1}$ and a step size of 0.01° in 2θ range ($20\text{--}80^\circ$). The N_2 -sorption isotherms were measured at $-196 \text{ }^\circ\text{C}$ with a TriStar II 3020 surface area analyzer (Micromeritics Inc., Norcross, GA, UAS). Before measurement, the sample was degassed in a vacuum at 300 °C for 4 h. Raman spectra of the samples were collected using high-resolution Raman spectroscopy (LabRAM HR Evolution visible_NIR, HORIBA) with a 514 nm laser in the range of $100\text{--}3500 \text{ cm}^{-1}$. The Pt contents of the samples were measured using ICP-OES (PerkinElmer AVIO500, Waltham, MA, USA). Thermogravimetry (TG) measurement was conducted using a SETARAM apparatus at a heating rate of $10 \text{ }^\circ\text{C} \cdot \text{min}^{-1}$ from 40 to 800 °C under air flow ($10 \text{ mL} \cdot \text{min}^{-1}$).

2.4. Gas-Sensing Measurement

The gas-sensing measurement system used was a laboratory-made system that could control working temperature, humidity level, and analyte gas concentration inside the reaction chamber. The fabricated gas sensor was located in the reaction chamber in the measurement system. Then, 20 ppm formaldehyde (RIGAS Co., Daejeon, Republic of Korea) gas was used as the analyte gas and diluted from 50 to 1000 ppb with dry air as the balance gas via mass flow controllers

Based on the requirements, humid air was supplied through a humidity chamber and temperature was controlled (by halogen lamp) in the chamber. To check the performance of the gas sensor, the electric resistance was measured and recorded with a digital system (Agilent 34970A, Culver, CA, USA). The performance of the gas sensor was primarily considered by its response value. The response (R) of a p-type semiconductor is calculated following Equation (1)

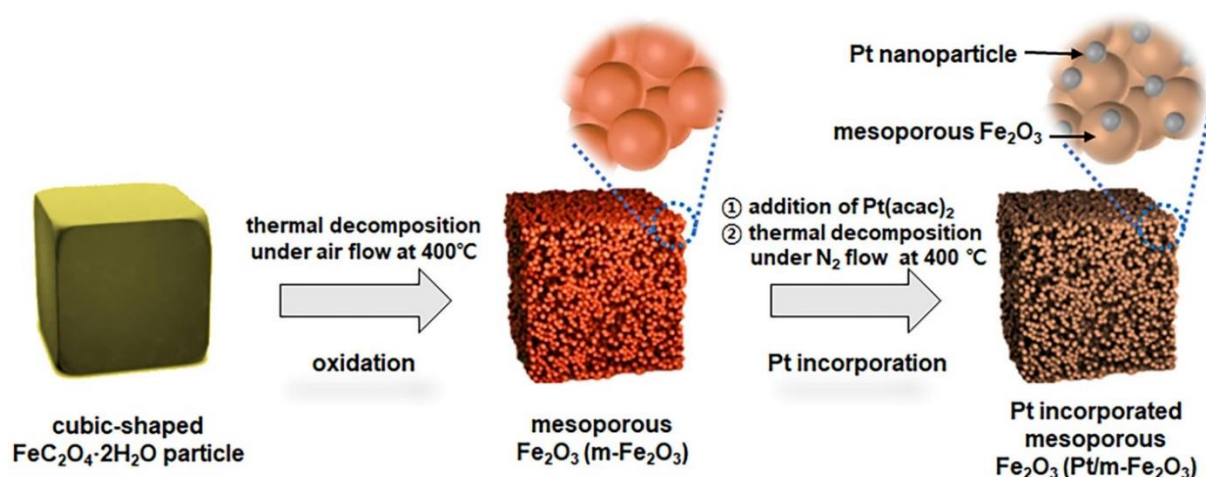
$$R = R_{gas}/R_{air} \quad (1)$$

where R_{gas} is the electric resistance when exposed to the target gas, and R_{air} is the electric resistance in air conditions without the target gas.

3. Results and Discussion

3.1. Synthesis of Pt-Incorporated Mesoporous Fe_2O_3

The incorporation of Pt NPs was simply conducted by mixing the Fe_2O_3 powder and $Pt(acac)_2$ followed by the thermal treatment of the mixture under an N_2 flow condition at 400 °C (Scheme 1). First, cubic-shaped $FeC_2O_4 \cdot 2H_2O$ particles could be obtained as a precursor of m- Fe_2O_3 from a hydrothermal reaction of $Fe(NO_3)_3 \cdot 9H_2O$ under the presence of PVP as a surfactant and glucose as a carbon source, as reported in previous work [33]. Additionally, the obtained $FeC_2O_4 \cdot 2H_2O$ powder could be decomposed and further oxidized to m- Fe_2O_3 particles via thermal oxidation under air flow at 400 °C. The weight ratio of the Pt precursor (g)/m- Fe_2O_3 powder (g) was 0.004 in the mixture, and the incorporated wt% of Pt was 0.2 in the Pt/m- Fe_2O_3 sample. The $Pt(acac)_2$ compound (m.p. = 249–252 °C) could be completely decomposed during thermal treatment at 400 °C, yielding highly dispersed Pt NPs deposited on the Fe_2O_3 surface.



Scheme 1. Brief scheme for the synthesis of the Pt/m- Fe_2O_3 microcubes.

The SEM image shows cubic-shaped Pt/m- Fe_2O_3 particles with crack-like large pores (Figure 1a). The average size of the Pt/m- Fe_2O_3 particles is observed to be $4.0 \pm 0.8 \mu m$ by measuring the edges of 200 particles in the SEM images (Figure 1b). The shape and size of Pt/m- Fe_2O_3 are similar to pristine m- Fe_2O_3 (Figure S1a–c, see Electronic Supplementary Information). The TEM image shows the edge of the cubic Pt/m- Fe_2O_3 consisting of small particles (approximately 25–30 nm) and pores (Figure 1c). The high-angle annular dark field (HAADF)-TEM image shows the uniform and high dispersion of Pt particles (<2 nm sizes)

on $m\text{-Fe}_2\text{O}_3$ (Figure 1d). The elemental mapping image of Pt (green color) and magnified TEM image demonstrate the uniform Pt distribution (Figure 1e,f). The high-resolution TEM (HR-TEM) image shows line spacings of 0.22 and 0.25 nm indexed to the Pt (111) and Fe_2O_3 (110) reflections, respectively (Figure 1g).

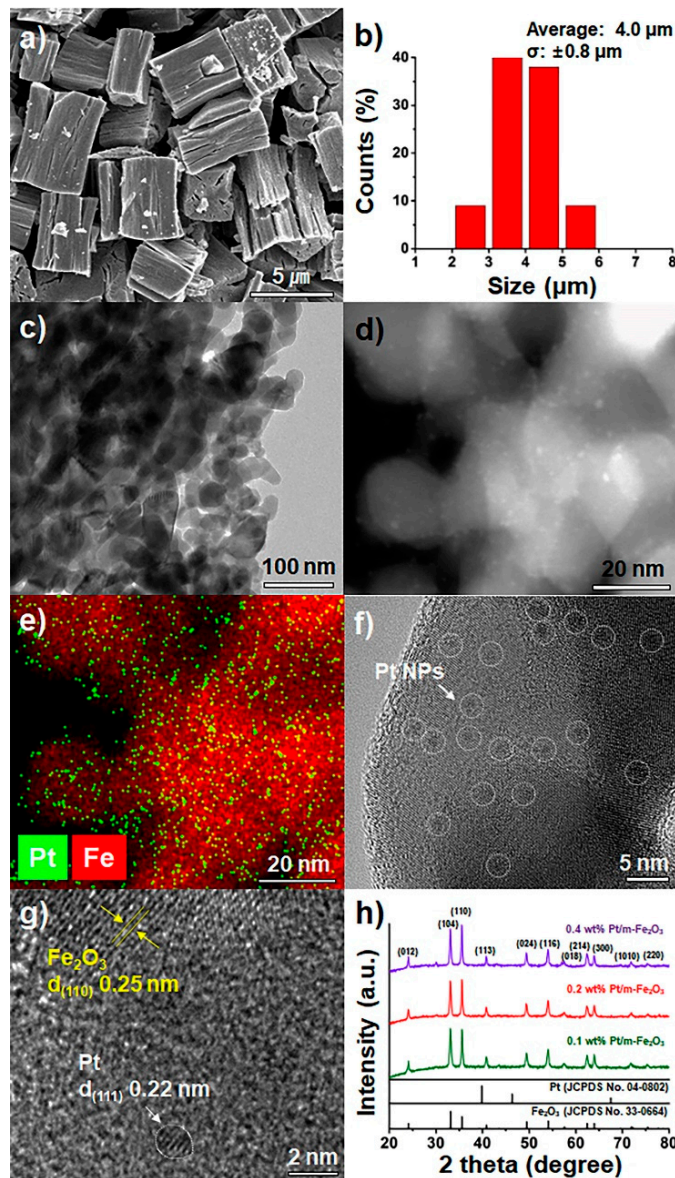


Figure 1. (a) SEM image; (b) particle size distribution histogram; (c) TEM image; (d) HAADF-STEM image; (e) elemental mapping image; (f) magnified TEM image; (g) HR-TEM image of 0.2 wt% Pt/ $m\text{-Fe}_2\text{O}_3$; and (h) XRD spectra of the Pt/ $m\text{-Fe}_2\text{O}_3$ samples.

The X-ray diffraction (XRD) patterns in all Pt/ $m\text{-Fe}_2\text{O}_3$ samples with the different Pt contents identically represent peaks at $2\theta = 24, 33,$ and 36° , assigned to the reflections of the (012), (104), and (110) planes of a Fe_2O_3 rhombohedral structure (Figure 1h, JCPDS No. 33-0664). In the XRD spectra, no significant difference was observed between Pt/ $m\text{-Fe}_2\text{O}_3$ and Pt-free $m\text{-Fe}_2\text{O}_3$ (Figure S1d). Using the Debye–Scherrer equation based on the peak broadening of the (110) reflection in the Pt-doped samples, the Fe_2O_3 crystal domain sizes were measured to be around 35 nm, which matched well with the size observed in the TEM images. The N_2 sorption experiment at -196°C for the Pt/ $m\text{-Fe}_2\text{O}_3$ exhibited type IV adsorption–desorption hysteresis (Figure 2a). The Brunauer–Emmett–Teller (BET) surface area and total pore volume were calculated to be $25\text{ m}^2\cdot\text{g}^{-1}$ and $0.13\text{ cm}^3\cdot\text{g}^{-1}$, respectively.

With the Barrett–Joyner–Halenda (BJH) method, the pore size in the Pt/m-Fe₂O₃ particle was determined to be 21 nm in the desorption branch (Figure 2b). Because well-defined pores and small crystals can improve gas-sensing performance, we assumed that forming m-Fe₂O₃ microcubes with a long-range ordered framework consisting of suitable hematite crystals and nanopores with large surface areas could contribute to the significant response to VOCs. We consider that m-Fe₂O₃ microcubes with a large surface area, small grain size, and large contact area are sensitive and reliable gas-sensing materials. Furthermore, the incorporation of small noble metal nanoparticles may result in significant synergy for VOC detection.

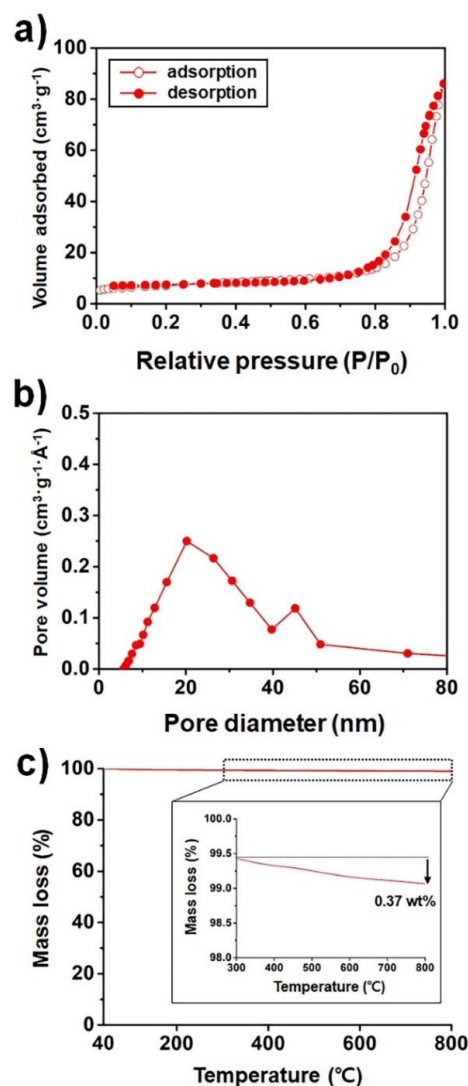


Figure 2. (a) N₂ sorption isotherms; (b) pore size distribution diagram; (c) TG curve of 0.2% Pt/m-Fe₂O₃.

In the thermogravimetric analysis (TGA), 0.2 wt% Pt/m-Fe₂O₃ showed a slight mass loss of 0.37 wt% in the range of 300 to 800 °C, demonstrating the presence of carbon residue in the sample (Figure 2c). Although this value is small, this showed a meaningful value similar to the ~0.24 wt% mass loss of p-type m-Fe₂O₃ published in the previous paper, which is different from the ~0 wt% mass loss of commercial n-type Fe₂O₃ nanoparticles [33]. We performed additional characterization experiments to confirm the carbon residue. However, any significant peaks for residual carbon were not detected in the Raman analysis, only showing the intrinsic peaks of α -Fe₂O₃ (Figure S2). A typical G band of carbon was not observed around 1560 cm⁻¹ due to the very high intensity of Fe₂O₃ and a small amount

of residual carbon. We believe that the presence of trace carbon impurities affecting the electric properties of Pt/m-Fe₂O₃ could be indirectly confirmed by TGA.

With inductively coupled plasma optical emission spectrometry (ICP-OES) measurements, the Pt contents in the nominal Pt/m-Fe₂O₃ samples were obtained to be 0.14 wt% at 0.1 wt% Pt/m-Fe₂O₃, 0.23 at 0.2 wt% Pt/m-Fe₂O₃, and 0.43 wt% at 0.4 wt% Pt/m-Fe₂O₃, respectively.

3.2. Performance of HCHO Gas Sensing

The 0.2% Pt/m-Fe₂O₃ and m-Fe₂O₃ sensing materials were prepared in a paste form by mixing them with glues, after which they were screen-printed onto interdigitated electrodes. After thermal treatment at 400 °C for 2 h, the fabricated gas sensors were investigated by an electrical resistance measurement system. The formaldehyde gas (20 ppm) samples were mixed with dry air to meet the desired analyte concentration, which was in the range of 50–1000 ppb, using mass flow controllers.

The working temperature has a significant influence on gas-sensing properties. As a well-known property of semiconductors, the resistance of Pt/m-Fe₂O₃ and m-Fe₂O₃ showed a gradual decrease with temperature increase. To determine the optimal concentration of Pt incorporation and suitable working temperature for the gas-sensing response, the pure m-Fe₂O₃ and several Pt/m-Fe₂O₃ samples (0.1, 0.2, and 0.4 wt% Pt-incorporated) were measured at different temperatures from 260 to 300 °C for 100 ppb HCHO gas. The response shape peaked at 275 °C, and 0.2% Pt/m-Fe₂O₃ was the most sensitive response, as shown in Figure 3. When the Pt content was higher than the optimal addition, the response was poor again due to the agglomeration of Pt [31]. Therefore, 0.2% Pt/m-Fe₂O₃ was selected, and 275 °C was decided as the working temperature for the investigations of the HCHO gas-sensing performance. Additionally, the HCHO gas response of 0.2% Pt/m-Fe₂O₃ was significantly higher than that of m-Fe₂O₃ at 275 °C.

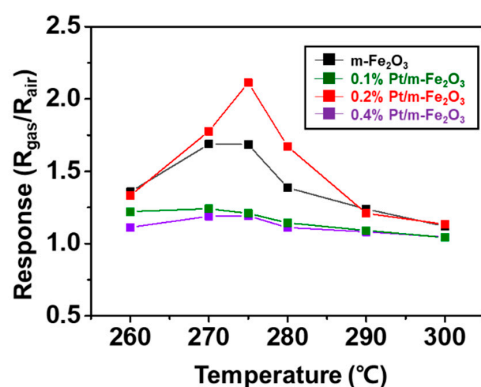


Figure 3. Response of m-Fe₂O₃ and Pt/m-Fe₂O₃ (0.1, 0.2, and 0.4 wt% Pt) operating temperature in the range 260–300 °C for 100 ppb HCHO gas.

Figure 4a shows the dynamic resistance change curves of 0.2% Pt/m-Fe₂O₃ and m-Fe₂O₃ to the HCHO gas in the range of 50–1000 ppb at 275 °C. In the initial air, the base resistance of 0.2% Pt/m-Fe₂O₃ was lower than that of m-Fe₂O₃ due to the electronic transition change after the addition of Pt [28]. Moreover, the 0.2% Pt/m-Fe₂O₃ had a larger resistance change ratio (response) than m-Fe₂O₃, while the target HCHO gas was injected (Figure 4b). Unlike other general Fe₂O₃ nanoparticles, our iron oxides (the Pt/m-Fe₂O₃ and m-Fe₂O₃) showed typical p-type electrical properties in which the resistance increased upon exposure to the HCHO gas. However, the conduction type of iron oxide was occasionally changed from n- to p-type when high temperatures were applied or impurities were added [34,35]. In a previous study, we discovered that exposing m-Fe₂O₃ to HCHO gas increased its resistance [33]. The presence of carbon impurities, which was the major cause of the p-type properties of the Pt/m-Fe₂O₃, can be expected by a mass loss of 0.2% Pt/m-Fe₂O₃ in the TGA (Figure 2c). Despite heat treatment at 400 °C, an extremely small amount of carbon residue remained in 0.2% Pt/m-Fe₂O₃, primarily originating from the

used PVP. Furthermore, the p-type properties of the gas sensors could be determined. We think that this was also shown by the more dynamic change obtained in terms of resistance with the increasing concentration of HCHO gas, whereby the response was better with a higher concentration of the target gas. Based on the resistance change, the response was calculated, as shown in Figure 4b. Additionally, the constant response for three consecutive measurements at 1000 ppb HCHO gas indicated the good repeatability of the gas sensing. The fitted line in Figure 4c depicts the relation between the response and concentration of HCHO gas at 275 °C. The responses of 0.2% Pt/m-Fe₂O₃ were 2.13, 2.60, 3.37, 3.96, 4.43, 5.19, 5.64, and 5.93 at 50, 100, 200, 300, 400, 600, 800, and 1000 ppb HCHO gas, respectively. We observed that the response of the 0.2% Pt/m-Fe₂O₃ was higher than that of the pristine m-Fe₂O₃ with a good linear shape. Particularly, response 2.13 at the low concentration of 50 ppb HCHO gas was very significant. The limit of detection (LOD) could be calculated following Equation (2) [36]:

$$\text{LOD} = 3\sigma/s \quad (2)$$

where σ is the standard deviation and s is the slope of the calibration curve. The result of the calculated LOD was 7.38 ppb at 0.2% Pt/m-Fe₂O₃ and 12.27 ppb at m-Fe₂O₃, implying that the 0.2% Pt/m-Fe₂O₃ gas sensor is more sensitive than the m-Fe₂O₃ sensor at extremely low concentration levels of HCHO gas. Details of the n- and p-type metal oxide semiconductor gas sensors are shown in Table 1.

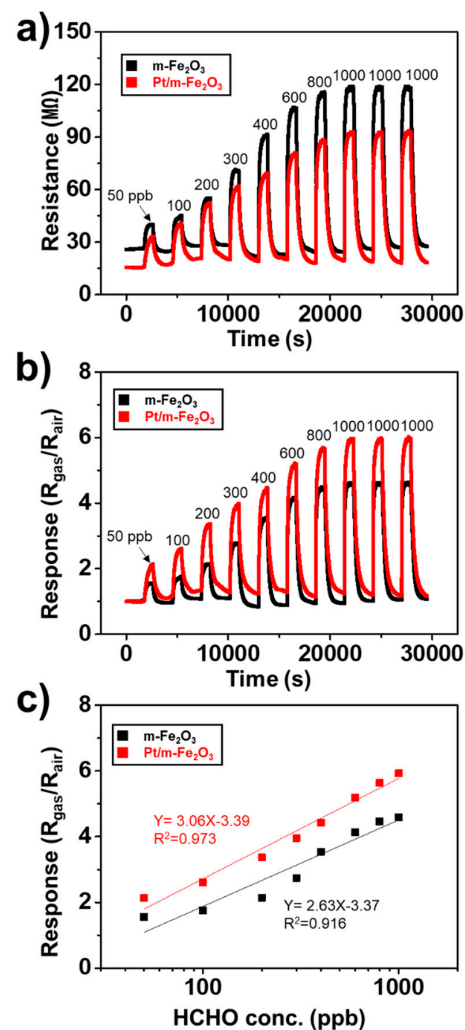


Figure 4. (a) Dynamic resistance changes in m-Fe₂O₃ and 0.2% Pt/m-Fe₂O₃; (b) response of m-Fe₂O₃ and 0.2% Pt/m-Fe₂O₃; and (c) linear fit between the response and log-scale HCHO concentration from 50 to 1000 ppb of m-Fe₂O₃ and 0.2% Pt-Fe₂O₃ at 275 °C.

Table 1. Comparisons of HCHO gas-sensing characteristics based on sensing materials.

Sensing Materials	Type	Temperature (°C)	Response/ppm	LOD (ppb)	Refs
Pt-SnO ₂	n-type	200	16/1	60	[37]
Ag-ZnO/In ₂ O ₃	n-type	260	186/100	9 *	[38]
La ₂ O ₃ -In ₂ O ₃	n-type	128	101.9/50	100	[39]
Al-doped ZnO	n-type	320	46.1/50	500	[40]
SnO ₂ /SnO	n-type	120	80.9/50	8.15 *	[41]
SnO ₂ /Fe ₂ O ₃	n-type	220	4.5/20	29 *	[42]
NiO/NiFe ₂ O ₄	p-type	240	22.5/100	200	[43]
Co ₃ O ₄ /CoFe ₂ O ₄	p-type	139	12.7/10	300 *	[44]
BiFeO ₃	p-type	260	10.5/20	80	[45]
LaFeO ₃	p-type	180	20.4/100	1000	[46]
m-Fe ₂ O ₃	p-type	275	1.12/0.05	-	[33]
Pt/m-Fe ₂ O ₃	p-type	275	2.13/0.05	7.38 *	This work

* calculated LOD.

Developing a good gas sensor is required to maintain high responses in high-humidity environments. Generally, metal oxide semiconductor gas sensors become less sensitive in such environments because water molecules adsorb on the sensing material surface rather than oxygen, and then the base resistance value increases [47,48] (Figure S3). The measurement in the humid environment was set at 200 ppb HCHO gas at 300 °C, rather than 275 °C, due to base resistance instability at high-humidity conditions. At 89% relative humidity (RH), the HCHO sensitivity performance of pristine m-Fe₂O₃ dropped to 48% compared to the dry air conditions. On the other hand, that of 0.2% Pt/m-Fe₂O₃ was only 25% lower in the same conditions. Even under the condition of 56% RH, similar properties of sensor performance are shown depending on changes in sensing materials, as in the case of 89% RH. The HCHO sensitivity performance of pristine m-Fe₂O₃ dropped to 35%, while that of 0.2% Pt/m-Fe₂O₃ decreased by only 18%, as shown in Figure 5a. Although high humidity unfortunately affects the sensitivity performance degradation of the gas sensor, the HCHO sensitivity performance of 0.2% Pt/m-Fe₂O₃ improved to nearly twice that of m-Fe₂O₃ at high-humidity conditions.

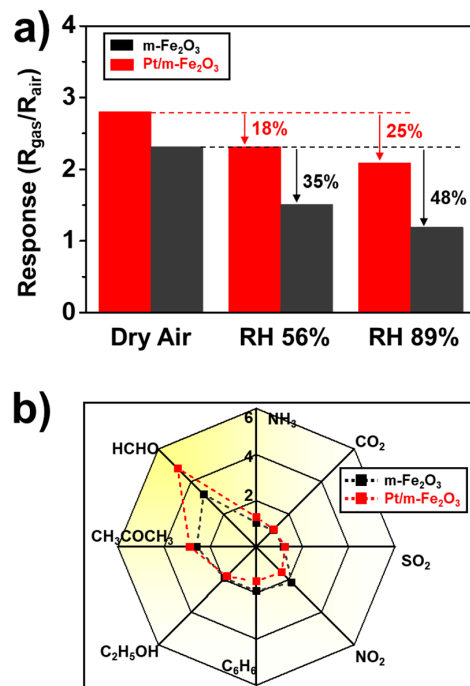


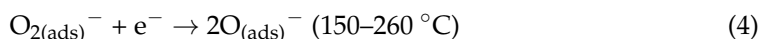
Figure 5. (a) Response of m-Fe₂O₃ and 0.2% Pt/m-Fe₂O₃ under different relative humidity (Dry air, RH 56% and RH 89%) with respect to the 200 ppb HCHO gas at 300 °C; (b) response of m-Fe₂O₃ and 0.2% Pt/m-Fe₂O₃ towards 500 ppb of several kinds of gases (concentration of CO₂ was 500 ppm) at 275 °C.

To determine the selectivity, several gases (HCHO, CH₃COCH₃, C₂H₅OH, C₆H₆, NO₂, SO₂, and NH₃) were tested at the same concentration at 500 ppb, except CO₂, which was tested at 500 ppm, and at the same temperature of 275 °C. Figure 5b indicates that 0.2% Pt/m-Fe₂O₃ and m-Fe₂O₃ showed good selectivity with HCHO gas. Additionally, the response ratio of HCHO against other gases ($R_{\text{HCHO}}/R_{\text{another gas}}$) of 0.2% Pt/m-Fe₂O₃ ranged from 1.68 to 4.50, whereas pristine m-Fe₂O₃ against other gases ($R_{\text{HCHO}}/R_{\text{another gas}}$) ranged from 1.25 to 3.26. The results show that the HCHO gas selectivity of 0.2% Pt/m-Fe₂O₃ is better than that of m-Fe₂O₃.

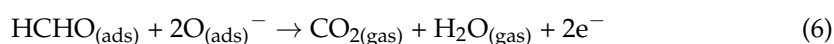
Practical applications require the long-term stability of gas sensors. To confirm the long-term stability of the 0.2% Pt/m-Fe₂O₃ gas sensor, it was consecutively measured with base resistance in air conditions for 120 h. The average resistance was 10.91 MΩ and standard deviation was 0.995. The response value at initial measurement was compared with responses after 90 and 120 days towards 500 ppb HCHO gas at 275 °C. The HCHO gas response was well maintained during this period (4.93 at initial test, 4.84 at 90 days, and 4.82 at 120 days, respectively), as shown in Figure S4. The long-term stability of the HCHO gas sensor, while having a high response to HCHO gas, was verified for 120 days. Additionally, the response and recovery times of 0.2% Pt/m-Fe₂O₃ to 500 ppb HCHO at 275 °C were measured to be 22 and 431 s, which was similar to m-Fe₂O₃ (63 and 395 s in previous results [33]).

3.3. Sensing Mechanism

When p-type semiconductors such as the Pt/m-Fe₂O₃ are exposed to ambient air, oxygen species are absorbed and ionized on the surface area of the sensing materials by capturing electrons (e⁻) and generating holes (h⁺) in the band of the sensing materials as [8]



If the reducing gases (such as HCHO) are in contact with the sensing materials, the ionized oxygen releases the electrons, and, subsequently, the released electrons are injected into the hole-accumulation area and recombine with holes as



Consequently, the change in the hole accumulation layer due to the reaction with the reducing gases leads to a resistance change because the charge carriers mainly move through the holes at the surface of the sensing materials.

Figure 6 depicts the sensing mechanism through the transition of the hole-accumulation layer of each sensing material (Pt/m-Fe₂O₃ and m-Fe₂O₃), as well as the contribution of Pt nanoparticles to enhance the sensitivity of HCHO gas sensing. Several studies have discussed the decisive role of noble metals as a catalyst because absorbed oxygen species in Pt nanoparticles could be ionized more easily, leading to a spill-over effect, while the surfaces of sensing materials respond to oxygen molecules [23,49,50]. The incorporated Pt nanoparticles might serve to increase the absorption and ionization of oxygen molecules by lowering the activation energy of the sensing material [37,40,51]. Figure 6a shows that Pt/m-Fe₂O₃ acquires a wider hole-accumulation layer than the pristine m-Fe₂O₃ in air conditions. The surface area of Pt/m-Fe₂O₃ has more ionized oxygen that could be reacted with the HCHO gas than the pristine m-Fe₂O₃. Figure 6b displays the narrowed hole-accumulation layer when the surface of the sensing material is in contact with the HCHO gas, and the degree of the reduction in the hole accumulation layer of Pt/m-Fe₂O₃ is bigger than that of m-Fe₂O₃. The sensitivity of the semiconductor gas sensors was decided at the scale of the resistance change, and depends on the extent of the surface reaction

between the sensing materials and the target gas. Therefore, Pt-incorporated nanoparticles in m-Fe₂O₃ play a critical role as enhancers.

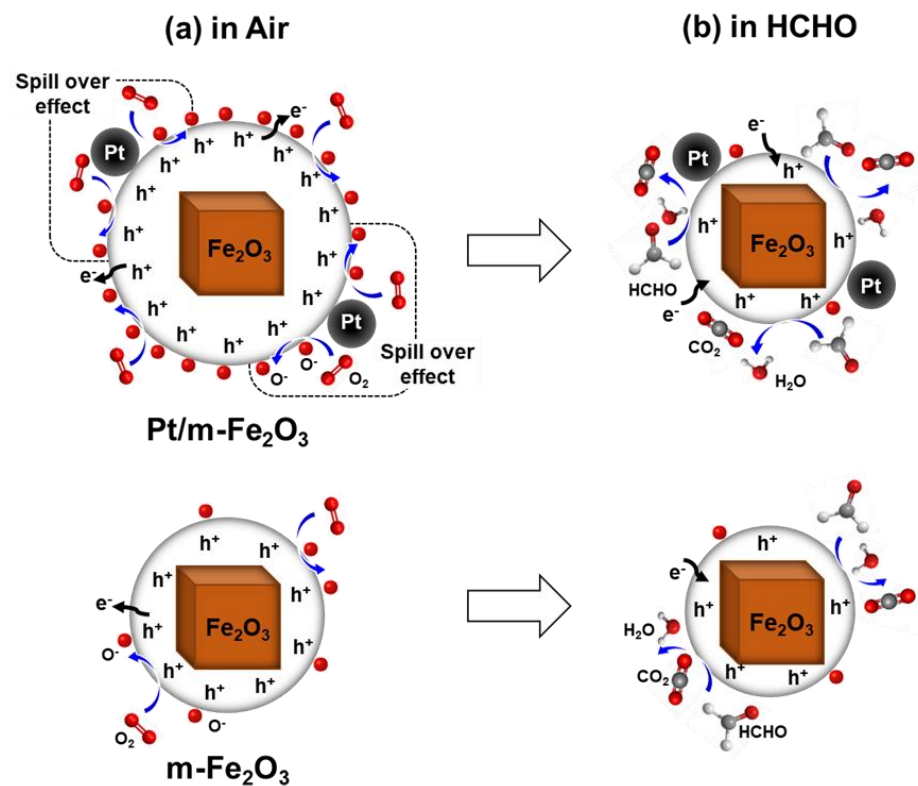


Figure 6. Schematic of gas-sensing mechanism for m-Fe₂O₃ and Pt/m-Fe₂O₃ (a) in air and (b) in HCHO conditions.

4. Conclusions

In this study, highly dispersed Pt-incorporated mesoporous Fe₂O₃ microcubes were synthesized as a p-type by the facile thermal treatment of mixture powders such as m-Fe₂O₃ and Pt precursor without harmful chemicals and inhomogeneous dispersion. Furthermore, electric studies of 0.2% Pt/m-Fe₂O₃ were conducted to confirm the properties of the HCHO gas sensor. The sensor had a higher sensitivity ($R = 2.13$ at 50 ppb HCHO), high selectivity to formaldehyde gas, high performance under high humidity conditions, and similar long-term stability (retention time of 120 days) compared with a previous m-Fe₂O₃ gas sensor. Particularly, the response of 0.2% Pt/m-Fe₂O₃ at the low-level formaldehyde gas concentration (50 ppb) improved by over 90% compared with our previous m-Fe₂O₃ because of the spill-over effect by the Pt NPs. The sensitivity performance of 0.2% Pt/m-Fe₂O₃ was almost twice as high as that of m-Fe₂O₃ in high-humidity conditions. This means that 0.2% Pt/m-Fe₂O₃ could be a good potential sensing material for HCHO gas for detecting very low ppb levels.

Supplementary Materials: The following supporting information can be downloaded at: <https://www.mdpi.com/article/10.3390/nano13040659/s1>, Figure S1: (a) SEM and (b) magnified SEM images, (c) TEM image, and (d) XRD spectrum of the m-Fe₂O₃; Figure S2: Raman spectra of the m-Fe₂O₃ and 0.2wt% Pt/m-Fe₂O₃; Figure S3: Resistance changes of the Pt/m-Fe₂O₃ under different relative humidity (Dry air, RH 56% and RH 89%) with respect to the 200 ppb HCHO gas at 300 °C; Figure S4: Base resistance of Pt-Fe₂O₃ in air condition for 120 h consecutively. (The insets were HCHO gas response of Pt-Fe₂O₃ toward 500 ppb HCHO gas at the initial test, after 90 days and 120 days at 275 °C).

Author Contributions: Conceptualization, Y.C., J.C.P. and H.J.P.; methodology, Y.C., J.C.P. and H.J.P.; validation, S.J.J. and K.H.O.; formal analysis, S.J.J. and K.H.O.; investigation, S.J.J. and K.H.O.; resources, J.C.P. and H.J.P.; data curation, S.J.J. and K.H.O.; writing—original draft preparation, S.J.J. and K.H.O.; writing—review and editing, Y.C., J.C.P. and H.J.P.; visualization, S.J.J. and K.H.O.; supervision, Y.C., J.C.P. and H.J.P.; project administration, J.C.P. and H.J.P.; funding acquisition, J.C.P. and H.J.P. All authors have read and agreed to the published version of the manuscript.

Funding: This work was supported by the National Research Foundation of Korea under research projects (NRF-2017M3A9F1033056) and the Institute of Information & Communications Technology Planning & Evaluation (IITP) grant funded by the Korean government (MSIT-2022-0-00025). It was also supported by the Research and Development Program of the Korean Institute of Energy Research (KIER) (No. C2-2454).

Conflicts of Interest: The authors declare no conflict of interest.

References

1. Gupta, K.; Ulsamer, A.; Preuss, P. Formaldehyde in indoor air: Sources and toxicity. *Environ. Int.* **1982**, *8*, 349–358.
2. Blondel, A.; Plaisance, H. Screening of Formaldehyde Indoor Sources and Quantification of Their Emission Using a Passive Sampler. *Buill. Environ.* **2011**, *46*, 1284–1291.
3. Park, H.J.; Choi, N.J.; Kang, H.; Jung, M.Y.; Park, J.W.; Park, K.H.; Lee, D.S. A ppb-level formaldehyde gas sensor based on CuO nanocubes prepared using a polyol process. *Sens. Actuators B Chem.* **2014**, *203*, 282–288.
4. Chi, C.Y.; Chen, H.I.; Chen, W.C.; Chang, C.H.; Liu, W.C. Formaldehyde sensing characteristics of an aluminum-doped zinc oxide (AZO) thin-film-based sensor. *Sens. Actuators B Chem.* **2018**, *255*, 3017–3024.
5. Agency for Toxic Substances and Disease Registry. Minimal Risk Levels (MRLs). 2022. Available online: <https://www.cdc.gov/TSP/MRLS/mrlslisting.aspx> (accessed on 15 August 2022).
6. Moseley, P.T. Progress in the development of semiconducting metal oxide gas sensors: A review. *Meas. Sci. Technol.* **2017**, *28*, 082001.
7. Han, Z.J.; Qi, Y.; Yang, Z.Y.; Han, H.C.; Jiang, Y.Y. Recent advances and perspectives on constructing metal oxide semiconductor gas sensing materials for efficient formaldehyde detection. *J. Mater. Chem. C* **2020**, *8*, 13169–13188. [[CrossRef](#)]
8. Lou, C.; Lei, G.; Liu, X.; Xie, J.; Li, Z.; Zheng, W.; Goel, N.; Kumar, M.; Zhang, J. Design and optimization strategies of metal oxide semiconductor nanostructures for advanced formaldehyde sensors. *Coord. Chem. Rev.* **2022**, *452*, 214280.
9. Ji, H.; Zeng, W.; Li, Y. Gas sensing mechanisms of metal oxide semiconductors: A focus review. *Nanoscale* **2019**, *11*, 22664–22684.
10. Dai, Z.; Liang, T.; Lee, J.H. Gas sensors using ordered macroporous oxide nanostructures. *Nanoscale Adv.* **2019**, *1*, 1626–1639. [[CrossRef](#)]
11. Prajesh, R.; Goyal, V.; Nahid, M.; Saini, V.; Singh, A.K.; Sharma, A.K.; Bhargava, J.; Agarwal, A. Nickel oxide (NiO) thin film optimization by reactive sputtering for highly sensitive formaldehyde sensing. *Sens. Actuators B Chem.* **2020**, *318*, 128166.
12. Kim, H.J.; Lee, J.H. Highly sensitive and selective gas sensors using p-type oxide semiconductors: Overview. *Sens. Actuators B Chem.* **2014**, *192*, 607–627. [[CrossRef](#)]
13. Kim, H.-J.; Choi, K.-I.; Kim, K.-M.; Na, C.W.; Lee, J.-H. Highly sensitive C₂H₅OH sensors using Fe-doped NiO hollow spheres. *Sens. Actuators B Chem.* **2012**, *171*, 1029–1037.
14. Yoon, J.-W.; Kim, H.-J.; Kim, I.-D.; Lee, J.-H. Electronic sensitization of the response to C₂H₅OH of p-type NiO nanofibers by Fe doping. *Nanotechnology* **2013**, *24*, 444005. [[PubMed](#)]
15. Wang, L.; Lou, Z.; Wang, R.; Fei, T.; Zhang, T. Ring-like PdO-decorated NiO with lamellar structures and their application in gas sensor. *Sens. Actuators B Chem.* **2012**, *171–172*, 1180–1185.
16. Kim, H.R.; Haensch, A.; Kim, I.D.; Barsan, N.; Weimar, U.; Lee, J.H. The Role of NiO Doping in Reducing the Impact of Humidity on the Performance of SnO₂-Based Gas Sensors: Synthesis Strategies, and Phenomenological and Spectroscopic Studies. *Adv. Funct. Mater.* **2011**, *21*, 4456–4463. [[CrossRef](#)]
17. Lee, J.H. Gas Sensors Using Hierarchical and Hollow Oxide Nanostructures: Overview. *Sens. Actuators B Chem.* **2009**, *140*, 319–336. [[CrossRef](#)]
18. Mirzaei, A.; Ansari, H.R.; Shahbaz, M.; Kim, J.-Y.; Kim, H.W.; Kim, S.S. Metal Oxide Semiconductor Nanostructure Gas Sensors with Different Morphologies. *Chemosensors* **2022**, *10*, 289.
19. Ren, P.; Qi, L.; You, K.; Shi, Q. Hydrothermal Synthesis of Hierarchical SnO₂ Nanostructures for Improved Formaldehyde Gas Sensing. *Nanomaterials* **2022**, *12*, 228.
20. Dey, A. Semiconductor metal oxide gas sensors: A review. *Mater. Sci. Eng. B* **2018**, *229*, 206–217. [[CrossRef](#)]
21. Chen, M.; Yin, H.; Li, X.; Qiu, Y.; Cao, G.; Wang, J.; Yang, X.; Wang, P. Facet- and defect-engineered Pt/Fe₂O₃ nanocomposite catalyst for catalytic oxidation of airborne formaldehyde under ambient conditions. *J. Hazard. Mater.* **2020**, *395*, 122628.
22. Huang, J.Y.; Liang, H.; Ye, J.X.; Jiang, D.T.; Sun, Y.L.; Li, X.J.; Geng, Y.F.; Wang, J.Q.; Qian, Z.F.; Du, Y. Ultrasensitive formaldehyde gas sensor based on Au-loaded ZnO nanorod arrays at low temperature. *Sens. Actuators B Chem.* **2021**, *346*, 130568.

23. Chen, W.C.; Niu, J.S.; Liu, I.P.; Ke, B.Y.; Cheng, S.Y.; Liu, W.C. Hydrogen sensing properties of a GaN/AlGaN-based Schottky diode with a catalytic platinum (Pt) hybrid structure. *Sens. Actuators B Chem.* **2021**, *331*, 129320–129330. [[CrossRef](#)]
24. Liu, C.; Gao, H.; Wang, L.; Wang, T.; Yang, X.; Sun, P.; Gao, Y.; Liang, X.; Liu, F.; Song, H.; et al. Facile synthesis and the enhanced sensing properties of Pt-loaded α -Fe₂O₃ porous nanospheres. *Sens. Actuators B Chem.* **2017**, *252*, 1153–1162. [[CrossRef](#)]
25. Ma, J.H.; Ren, Y.; Zhou, X.R.; Liu, L.L.; Zhu, Y.H.; Cheng, X.W.; Xu, P.C.; Li, X.X.; Deng, Y.H.; Zhao, D.Y. Pt Nanoparticles Sensitized Ordered Mesoporous WO₃ Semiconductor: Gas Sensing Performance and Mechanism Study. *Adv. Funct. Mater.* **2018**, *28*, 1705268. [[CrossRef](#)]
26. Liu, Y.; Gao, X.; Li, F.; Lu, G.; Zhang, T.; Barsan, N. Pt-In₂O₃ mesoporous nanofibers with enhanced gas sensing performance towards ppb-level NO₂ at room temperature. *Sens. Actuators B* **2018**, *260*, 927–936.
27. Wang, G.; Yang, S.; Cao, L.; Jin, P.; Zeng, X.; Zhang, X.; Wei, J. Engineering mesoporous semiconducting metal oxides from metal-organic frameworks for gas sensing. *Coord. Chem. Rev.* **2021**, *445*, 214086. [[CrossRef](#)]
28. Lei, Z.; Cheng, P.; Wang, Y.; Xu, L.; Lv, L.; Li, X.; Sun, S.; Hao, X.; Zhang, Y.; Zhang, Y.; et al. Pt-doped α -Fe₂O₃ mesoporous microspheres with low-temperature ultra-sensitive properties for gas sensors in diabetes detection. *Appl. Surf. Sci.* **2023**, *607*, 154558. [[CrossRef](#)]
29. Ruiz, A.; Arbiol, J.; Cirera, A.; Cornet, A.; Morante, J.R. Surface activation by Pt-nanoclusters on titania for gas sensing applications. *Mater. Sci. Eng. C* **2002**, *19*, 105–109. [[CrossRef](#)]
30. Bai, Z.X.; Dong, W.H.; Ren, Y.P.; Zhang, C.; Chen, Q. Preparation of Nano Au and Pt Alloy Microspheres Decorated with Reduced Graphene Oxide for Nonenzymatic Hydrogen Peroxide Sensing. *Langmuir* **2018**, *34*, 2235–2244. [[CrossRef](#)]
31. Lin, B.; Jia, F.; Lv, B.; Qin, Z.; Liu, P.; Chen, Y. Facile synthesis and remarkable hydrogen sensing performance of Pt-loaded SnO₂ hollow microspheres. *Mater. Res. Bull.* **2018**, *106*, 403–408.
32. Liu, Y.; Huang, J.; Yang, J.; Wang, S. Pt nanoparticles functionalized 3D SnO₂ nanoflowers for gas sensor application. *Solid. State. Electron.* **2017**, *130*, 20–27. [[CrossRef](#)]
33. Park, H.J.; Hong, S.Y.; Chun, D.H.; Kang, S.W.; Park, J.C.; Lee, D.S. A highly susceptible mesoporous hematite microcube architecture for sustainable P-type formaldehyde gas sensors. *Sens. Actuators B Chem.* **2019**, *287*, 437–444. [[CrossRef](#)]
34. Gurlo, A.; Bărsan, N.; Oprea, A.; Sahm, M.; Sahm, T.; Weimar, U. An n- to p-type conductivity transition induced by oxygen adsorption on α -Fe₂O₃. *Appl. Phys. Lett.* **2004**, *85*, 2280–2282.
35. Barsan, N.; Simion, C.; Heine, T.; Pokhrel, S.; Weimar, U. Modeling of sensing and transduction for p-type semiconducting metal oxide based gas sensors. *J. Electroceram.* **2010**, *25*, 11–19. [[CrossRef](#)]
36. Shrivastava, A.; Gupta, V. Methods for the determination of limit of detection and limit of quantitation of the analytical methods. *Chronicles Young Sci.* **2011**, *2*, 21.
37. Tang, Y.; Han, Z.; Qi, Y.; Yang, Z.; Han, H.; Jiang, Y.; Zhang, X.; Wu, L.; Wang, Z.; Liu, J.; et al. Enhanced ppb-level formaldehyde sensing performance over Pt deposited SnO₂ nanospheres. *J. Alloys Compd.* **2022**, *899*, 163230.
38. Liu, J.; Zhang, L.; Cheng, B.; Fan, J.; Yu, J. A high-response formaldehyde sensor based on fibrous Ag-ZnO/In₂O₃ with multi-level heterojunctions. *J. Hazard. Mater.* **2021**, *413*, 125352.
39. Zeng, X.; Liu, L.; Lv, Y.; Zhao, B.; Ju, X.; Xu, S.; Zhang, J.; Tian, C.; Sun, D.; Tang, X. Ultra-sensitive and fast response formaldehyde sensor based on La₂O₃-In₂O₃ beaded nanotubes at low temperature. *Chem. Phys. Lett.* **2020**, *746*, 137289.
40. Khojier, K. Preparation and investigation of Al-doped ZnO thin films as a formaldehyde sensor with extremely low detection limit and considering the effect of RH. *Mater. Sci. Semicond. Process.* **2021**, *121*, 105283.
41. Li, N.; Fan, Y.; Shi, Y.; Xiang, Q.; Wang, X.; Xu, J. A low temperature formaldehyde gas sensor based on hierarchical SnO/SnO₂ nano-flowers assembled from ultrathin nanosheets: Synthesis, sensing performance and mechanism. *Sens. Actuators B Chem.* **2019**, *294*, 106–115.
42. Lou, C.; Huang, Q.; Li, Z.; Lei, G.; Liu, X.; Zhang, J. Fe₂O₃-sensitized SnO₂ nanosheets via atomic layer deposition for sensitive formaldehyde detection. *Sens. Actuators B Chem.* **2021**, *345*, 130429.
43. Xu, Y.; Tian, X.; Fan, Y.; Sun, Y. A formaldehyde gas sensor with improved gas response and sub-ppm level detection limit based on NiO/NiFe₂O₄ composite nanotetrahedrons. *Sens. Actuators B Chem.* **2020**, *309*, 127719. [[CrossRef](#)]
44. Zhang, N.; Ruan, S.; Qu, F.; Yin, Y.; Li, X.; Wen, S.; Adimi, S.; Yin, J. Metal-organic framework-derived Co₃O₄/CoFe₂O₄ double-shelled nanocubes for selective detection of sub-ppm-level formaldehyde. *Sens. Actuators B Chem.* **2019**, *298*, 126887.
45. Zhang, Y.F.; Li, J.Y.; Peng, L.; Ma, M.; Gao, D.J.; Bi, J.; Wu, J.T. Formaldehyde sensing with a parts-per-billion limit of detection by dielectric properties and crystal symmetry optimization in BiFeO₃-based p-type solid solution. *Sens. Actuators B Chem.* **2021**, *344*, 130314. [[CrossRef](#)]
46. Zhu, L.; Wang, J.A.; Liu, J.W.; Chen, X.; Xu, Z.C.; Ma, Q.Y.; Wang, Z.; Liang, J.D.; Li, S.S.; Yan, W. Designing highly sensitive formaldehyde sensors via A-site cation deficiency in LaFeO₃ hollow nanofibers. *Appl. Surf. Sci.* **2022**, *590*, 153085. [[CrossRef](#)]
47. Yang, M.; Lu, J.; Wang, X.; Zhang, H.; Chen, F.; Sun, J.; Yang, J.; Sun, Y. Acetone sensors with high stability to humidity changes based on Ru-doped NiO flower-like microspheres. *Sens. Actuators B Chem.* **2020**, *313*, 127965. [[CrossRef](#)]
48. Zhang, S.; Geng, W.; He, X.; Tu, J.; Ma, M.; Duan, L.; Zhang, Q. Humidity sensing performance of mesoporous CoO(OH) synthesized via one-pot hydrothermal method. *Sens. Actuators B Chem.* **2019**, *280*, 46–53. [[CrossRef](#)]
49. Lee, J.E.; Kim, D.Y.; Lee, H.K.; Park, H.J.; Ma, A.; Choi, S.Y.; Lee, D.S. Sonochemical synthesis of HKUST-1-based CuO decorated with Pt nanoparticles for formaldehyde gas-sensor applications. *Sens. Actuators B Chem.* **2019**, *292*, 289–296.

50. Dong, C.J.; Li, Q.; Chen, G.; Xiao, X.C.; Wang, Y.D. Enhanced formaldehyde sensing performance of 3D hierarchical porous structure Pt-functionalized NiO via a facile solution combustion synthesis. *Sens. Actuators B Chem.* **2015**, *220*, 171–179. [[CrossRef](#)]
51. Koo, A.; Yoo, R.; Woo, S.P.; Lee, H.-S.; Lee, W. Enhanced acetone-sensing properties of Pt-decorated Al-doped ZnO nanoparticles. *Sens. Actuators B Chem.* **2019**, *280*, 109–119. [[CrossRef](#)]

Disclaimer/Publisher’s Note: The statements, opinions and data contained in all publications are solely those of the individual author(s) and contributor(s) and not of MDPI and/or the editor(s). MDPI and/or the editor(s) disclaim responsibility for any injury to people or property resulting from any ideas, methods, instructions or products referred to in the content.